PRE-PRINT

Published paper available at
https://www.sciencedirect.com/science/article/pii/S0168169918317551

https://doi.org/10.1016/j.compag.2020.105248

Assessing the fidelity of Landsat-based fAPAR models in two diverse sugarcane growing regions

Contact: avn@sun.ac.za

Assessing the fidelity of Landsat-based fAPAR models in two diverse sugarcane growing regions

S.J. Muller[a], P. Sithole[b], A.Singels[b,c] and A. Van Niekerk[a]

[a]Department of Geography and Environmental Studies, University of Stellenbosch, Stellenbosch, South Africa
[b]South African Sugarcane Research Institute, Mount Edgecombe, South Africa
[c]Department of Plant and Soil Sciences, University of Pretoria, Pretoria, South Africa

HIGHLIGHTS

- Linear SWIR-based NDMI and AFRI models predicted fAPAR for irrigated and rainfed sugarcane most accurately.
- Calibrated NDVI models performed marginally better than published models for estimating fAPAR.
- Machine learning did not significantly improve estimation accuracy.
- fAPAR models performed better in irrigated production areas than in rainfed areas.

ABSTRACT

Sugarcane is a globally important crop used for producing sugar and for generating renewable energy. Timely and accurate forecasts of sugarcane yield and production are needed to optimize supply chain operations. Crop growth models (CGMs) are frequently used for sugarcane yield forecasting and have been shown to benefit from using remotely sensed data to force (calibrate) biophysical state variables, such as the fraction of absorbed photosynthetically active radiation (fAPAR). Little is known about the robustness of multispectral vegetation indices for modelling fAPAR in sugarcane growing regions were environmental conditions and farming practices are diverse. This study investigated how the relationships between multispectral Landsat-8 satellite imagery and in situ sugarcane fAPAR measurements vary over large heterogeneous areas. Specifically, it examined which spectral bands and indices are most appropriate for modelling fAPAR under particular production environments and assessed the robustness of the models for application in areas where sugarcane is grown under varying agro-climatic conditions. It was found that cropping and environmental conditions were the main drivers of sugarcane fAPAR modelling success. Significantly (40%) lower mean root mean squared errors (RMSEs) values were recorded in Pongola, which is attributed to the relatively homogenous conditions under which sugarcane is being grown in this area. Generally, the Sezela models were much weaker and the normalized difference vegetation index (NDVI) and soil-adjusted vegetation index (SAVI) models performed relatively poorly, with the best performing models being dominated by the SWIR bands and/or indices generated from it. The non-linear models dominated and are thus recommended for operational implementation owing to their relative simplicity and robustness. From these results we conclude that the use of remotely sensed data for estimating fAPAR throughout the growing season is highly beneficial, but that the selection of suitable variable (index) is critical, especially when the sugarcane area being considered is diverse in terms of farming practices, terrain and climate.

KEYWORDS

Sugarcane, fIPAR, fAPAR, remote sensing, satellite images, Landsat, radiation interception, crop canopy, vegetation index, model

1. INTRODUCTION

Sugarcane is grown in more than a hundred countries around the world. In 2016, global sugarcane production amounted to 1 890 million tons valued at US$ 92 billion, harvested from 27 million ha at an average yield of 70 t/ha (FAO, 2018). The main products from sugarcane are sugar and renewable energy in the form of bio-ethanol and bio-electricity and is a major contributor to the economy in countries such as Brazil, China, India, Pakistan, Thailand and South Africa (FAO, 2018). Timely and accurate forecasts of sugarcane yield and production are needed to optimize operational and resource use efficiencies along the supply chain. This includes planning and managing field production, harvesting, transport, milling, storage, delivery and marketing operations. Crop growth models (CGMs) are frequently used for sugar cane yield forecasting. Specifically, CGMs predict the impact of recent weather and water supply on current crop status and calculate the impacts of likely future weather and irrigation water supply on yields (Bezuidenhout and Singels, 2007; De Wit et al., 2010; Everingham et al., 2002, 2009; Morell et al., 2016). CGMs generally deliver good yield estimations, especially when the variation in species and physiological parameters and different cropping styles are taken into account. However, CGMs often assume ideal agronomic conditions and do not consider growth limitations due to pests, diseases, weeds, poor irrigation scheduling or nutritional deficits (e.g. salinity) (Jarmain et al., 2014; Morel et al., 2014). Ideally, CGMs should be calibrated with in situ biophysical measurements to represent the actual state of development of the crop. Collecting such data on a regular basis is not always cost-effective, especially when large areas are being considered. The alternative is to incorporate remotely sensed biophysical derivatives into CGMs to more accurately represent the actual state of the crop. This is done by either directly replacing (known as forcing) or calibrating so called “state variables” in the CGM with satellite derived biophysical variables (Jin et al., 2018, 2017; Morel et al., 2014; Moulin et al., 1998).

A state variable widely used in CGMs is the leaf area index (LAI), which is the one sided leaf area per unit projected ground area (Jones and Vaughan, 2010). Examples of CGMs coupled with remotely derived LAI for specific crop types include the ROTASK (Clevers et al., 2002) and WOFOST (Huang et al., 2015) models for wheat and the CERES model for maize and wheat (Fang et al., 2011; Jin et al., 2016; Li et al., 2015). A sugarcane specific CGM, called MOSICAS, was implemented by Bappel et al. (2005). They showed that forcing the model with LAI (derived from SPOT 4 & 5) reduced the root mean squared errors (RMSEs) of sugarcane yield prediction from 19 t/ha to 13 t/ha. Morel et al. (2014) similarly implemented MOSICAS by using the fraction of intercepted photosynthetically active radiation (fIPAR) derived from SPOT imagery to force the state variable. They found that this forcing improved the sugarcane yield prediction RMSE from 14.8 t/ha to 12.2 t/ha. By further optimizing the radiation use efficiency parameter, Morel et al. (2014) reduced the RMSE to 10.5 t/ha. Jarmain et al. (2014)

experimented with forcing the CANESIM model (Singels and Paraskevopoulos, 2017) with remote sensing estimates of fractional canopy cover, evapotranspiration (ET), ET deficit (defined as the difference between potential and actual ET) and aboveground biomass. They found that forcing with NDVI derived canopy cover performed the best and improved the sugarcane yield prediction by as much as 13% and consistently outperformed forcing with other biophysical variables.

From the examples above it is clear that forcing or calibrating CGMs with remotely sensed state variables can significantly improve yield predictions, but that the choice of variable is critical. Biophysical variables such as LAI and fraction of absorbed photosynthetically active radiation (fAPAR) seem to be most popular. The relationship between these two variables can be described using an equation based on Beer's law:

$$fAPAR = fAPAR_{max}(1 - e^{-k.LAI}) \quad \text{Equation 1}$$

Where $fAPAR_{max}$ ranges from 0.93 to 0.97 (Baret et al., 1989) and the radiation extinction coefficient k for sugarcane can range between 0.31 and 0.85 (De Silva and De Costa, 2012). There seems to be a general agreement that there is a stronger empirical relationship between fAPAR and remotely sensed derivatives (e.g. vegetation indices (VIs)) than between LAI and VIs (Fensholt and Sandholt, 2003). This is attributed to the strong linear correlation between VIs and fAPAR, whereas the relationship between VIs and LAI is often non-linear (Nguy-Robertson et al., 2012). LAI is also known to saturate at high canopy-cover densities (Jones and Vaughan, 2010).

fAPAR is derived from photosynthetically active radiation (PAR) – wavelengths from 400 to 700 nm – and is absorbed during photosynthesis. The absorbed PAR (APAR) consists of four components namely: 1) the incidence PAR (INPAR); 2) INPAR that is transmitted through the canopy (TPAR); 3) TPAR that is reflected by the soil back to the canopy ($RPAR_s$); and 4) TPAR and INPAR that is reflected away by the soil and on top of the canopy ($RPAR_{cs}$) (Bastiaanssen and Ali, 2003). These components interact in the following manner:

$$APAR = (INPAR + RPAR_s) - (TPAR + RPAR_{cs}) \quad \text{Equation 2}$$

The fraction of absorbed PAR (fAPAR) provides information about a canopy's' functioning and is an indicator of a plant's productivity (Jones and Vaughan, 2010). There is a slight difference between the fraction of absorbed (fAPAR) and fraction of intercepted (fIPAR) PAR of canopies. fIPAR only accounts for the INPAR and TPAR components and assumes that $RPAR_s$ and $RPAR_{cs}$ have relatively small influences on the APAR–TPAR relationship (Gallo and Daughtry, 1986). However, the difference between the fIPAR and fAPAR is small at high proportions of canopy cover as about 94% of the fIPAR is absorbed by the canopy under such conditions (Gallo and Daughtry, 1986; Jones and Vaughan, 2010; Ridao et al., 1998). fIPAR and fAPAR are consequently often used interchangeably in agronomy and specifically in CGMs, but fAPAR is generally preferred as it accounts for the effects of dead leaves, stems and soil reflectance (Gallo et al., 1993; Ridao et al., 1998). To prevent ambiguity, the fraction of

absorbed/intercepted PAR will from hereon be referred to as fAPAR as it was assumed that the $RPAR_s$ and the $RPAR_{cs}$ components had minimal effect.

fAPAR can be derived from remotely sensed data by using either a physical radiative transfer model or an empirically derived relationship (Moulin et al., 1998). The MODIS based MOD15 (Myneni, 1997) and the SPOT VEGETATION based CYCLOPES fAPAR (Baret et al., 2007) are examples of fAPAR products derived from remotely sensed radiative transfer models. These products use VIs and land cover information to represent canopy cover characteristics, which is used to physically model fAPAR values. An alternative remote sensing approach for estimating fAPAR is based on empirical models that relate in situ measurements to multispectral data (often VIs). Most of these examples are crop-specific and include models for maize (Gitelson et al., 2014); wheat (Hatfield et al., 1984); beans (Gitelson et al., 2014); cereals (Myneni, 1997); sunflower (Joel et al., 1997); and lucern (Epiphanio and Huete, 1995). Comparatively few studies have attempted to model the fAPAR of sugarcane. Notable exceptions include Morel et al. (2014a) who employed NDVI derived from SPOT 4&5 images to produce a linear regression model for estimating the fAPAR of sugarcane fields in Reunion. They obtained a model with an R^2 of 0.9 and RMSE of 9 %. In a similar study, Zhang et al. (2015) used NDVI derived from Landsat 7 images to derive a linear regression model of fAPAR of sugar cane fields in Maui, which resulted in a model with an R^2 of 0.97 and RMSE of 4 %.

The near-linear relationship between fAPAR and VIs is influenced by a number of external factors. Empirical and radiative transfer models have shown that effects such as atmospheric conditions, view angle geometry, leaf angle distribution (LAD), canopy heterogeneity, reflectance interactions between soil-and-canopy and varying solar illumination geometry all play a significant role in the relationship between fAPAR and remotely sensed variables. This has led to suggestions that a single VI-fAPAR relationship cannot reliably be applied anywhere or at any time and that the relationship must be calibrated per site. Furthermore, VI-fAPAR relationships have shown non-linear traits at high canopy cover levels due to saturation (Rahman and Lamb, 2017) and at very low canopy cover levels due to soil reflectance interference (Jiang et al., 2006).

Canopy development of sugarcane varies and is a function of genotype (Singels and Donaldson, 2000; Zhou et al., 2003), environmental conditions (i.e. temperature) (Campbell et al., 1998; Inman-Bamber, 1994) and farming practices (e.g. row spacing) (Singels et al., 2005; Singels and Smit, 2002). Given these complications it is not clear to what extent remotely sensed data can effectively be used for operational monitoring of sugarcane fAPAR over large areas with different climatic conditions and where sugarcane is grown under diverse farming practices (e.g. irrigated vs. rainfed and varying row spacing). In addition, VIs such as NDVI are known to be affected by background reflection of soil and often saturates at high canopy cover levels. These effects are particularly problematic for monitoring sugarcane because canopies range from being open (during planting and after harvesting which introduces background reflection) to being fully closed (before harvest which could introduce saturation effects). Although attempts have been made to reduce the effects of background noise in vegetation indices (e.g. by using the soil-adjusted vegetation index (A.R. Huete, 1988)) and to counter the effect

of saturation (e.g. MTVI^2 (Haboudane et al., 2004)), it is not known whether such approaches will improve the accuracy and robustness of sugarcane fAPAR models in complex growing conditions. To date, no research has assessed various multispectral indices (that may be less affected by soil background and spectral saturation and may include the short wave infrared region (SWIR) for sugarcane fAPAR modelling. There is also a need to investigate the non-linear (e.g. exponential) or non-parametric (e.g. machine learning algorithms) traits in fAPAR modelling given the variations in sugarcane canopies.

The aim of this study is to investigate how the relationships between multispectral imagery and in situ sugarcane fAPAR measurements vary over a large and complex area. The multispectral bands of Landsat-8, along with a range of vegetation indices, are statistically compared to field measurements taken over two very diverse (in terms of climatic and geographic conditions and farming practices) sugarcane-growing areas in South Africa. The results are presented separately per study area and in combination to 1) investigate whether specific bands and indices perform better under certain production conditions and to 2) assess the robustness of models when applied to such large and complex areas. The article concludes with recommendations of how multispectral imagery can be used for operational sugarcane growth modelling and yield predictions, particularly within the context of the increased availability of high temporal (5-day revisit) and spatial (10m) resolution imagery that has recently become available through the European Space Agency's Copernicus Programme. Remaining challenges of the use of remotely sensed data for sugarcane yield forecasting are also highlighted.

2. METHODS

2.1 Study areas

Two sugarcane growing regions within South Africa were chosen as study areas. The first area consists of about 4500 fully irrigated sugarcane fields supplying the Pongola sugarcane mill in northern KwaZulu-Natal province, while the second area encompasses about 5500 rainfed fields supplying cane to the Sezela mill in the South Coast region of KwaZulu-Natal.

In Pongola (27°24'0" S, 31°35'0" E, 308 MASL) (Figure 1), the growing period of sugarcane is typically 12 months, with harvesting occurring from April to December. The climate is characterized by warm summer days (mean daytime temperature of 25 °C during January) and cool winter nights (mean minimum temperature for July of 8 °C), averaging to a mean annual temperature (MAT) of 20.7 °C. The area receives relatively low rainfall (mean annual precipitation, MAP, of 707mm), which is concentrated during summer. The low rainfall combined by a high evaporative demand (mean annual evaporation, MAE, of 1336 mm) (Figure 2) necessitates irrigation. The most dominant form of irrigation is overhead sprinkler systems, followed by centre pivot and drip irrigation systems.

The Sezela mill supply area consists of a warm (MAT of 20.6 °C) coastal region and a cooler (MAT of 19.4 °C) high-lying, inland section. The coastal climate is characterized by relatively high rainfall (MAP of 1080 mm), concentrated from October to December, which provides water sufficient for sustaining

rainfed sugarcane production. Sugarcane is also grown under rainfed conditions in the cooler, high lying inland region, referred to as the Paddock area. The limited supply of water, along with the cooler temperatures, results in relatively long growing periods (18 – 24 months), compared to the shorter growing periods of the coastal area (12 to 14 months).

The terrain of the Pongola and Sezela regions is another important distinguishing factor. The topography in Pongola is relatively flat (mean slope gradient, MSG, of 2.5°, standard deviation of 1.5°), while the landscape in Sezela is undulating (MSG of 8.9°, standard deviation of 5°). The relatively complex terrain of Sezela introduces variation in both the satellite imagery (i.e. illumination differences) and the growing conditions (i.e. terroir). These differences in terrain translates to the shapes and sizes of the fields within the two areas, with the irrigated fields in Pongola being larger and generally geometrically shaped (Figure 1), while the rainfed fields of Sezela (both in the coastal and Paddock sections) tend to be smaller with irregular, contour-following boundaries (Figure 2). The shapes and sizes of fields are relevant because small, narrow fields are problematic for the retrieval of remotely sensed information as it leads to increases in mixed pixels (Lebourgeois et al., 2017), especially when the instantaneous field of view (spatial resolution) of the imagery is not substantially smaller than the field size.

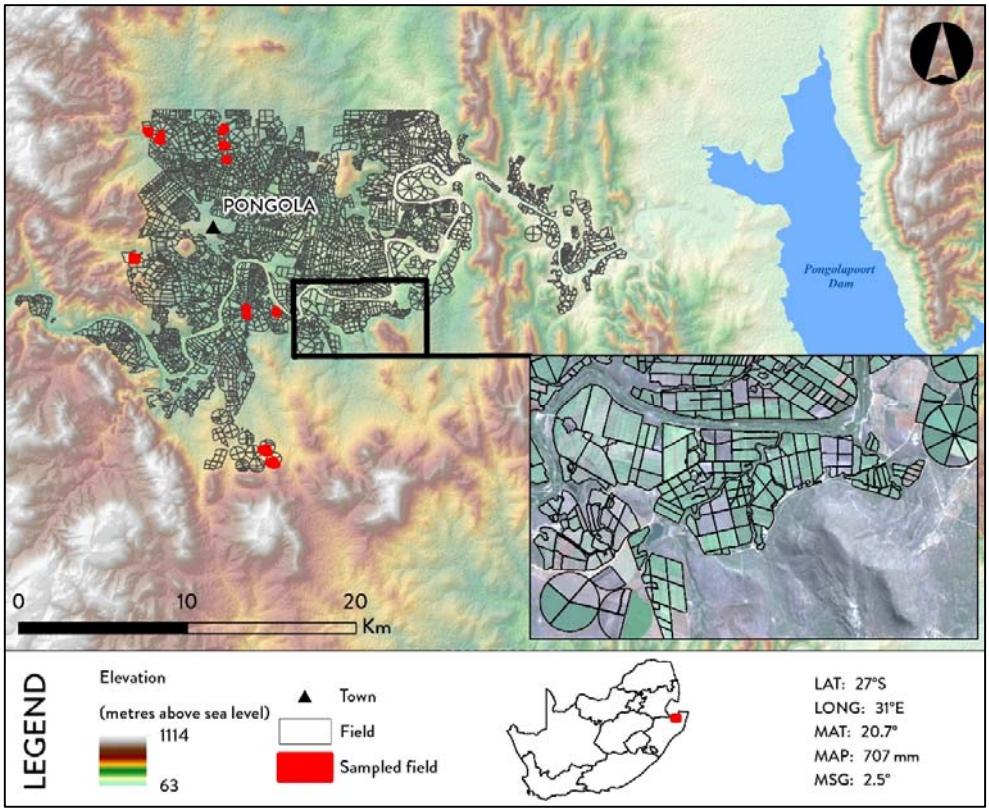

Figure 1 Pongola study area with an example of its larger, geometrical field structures

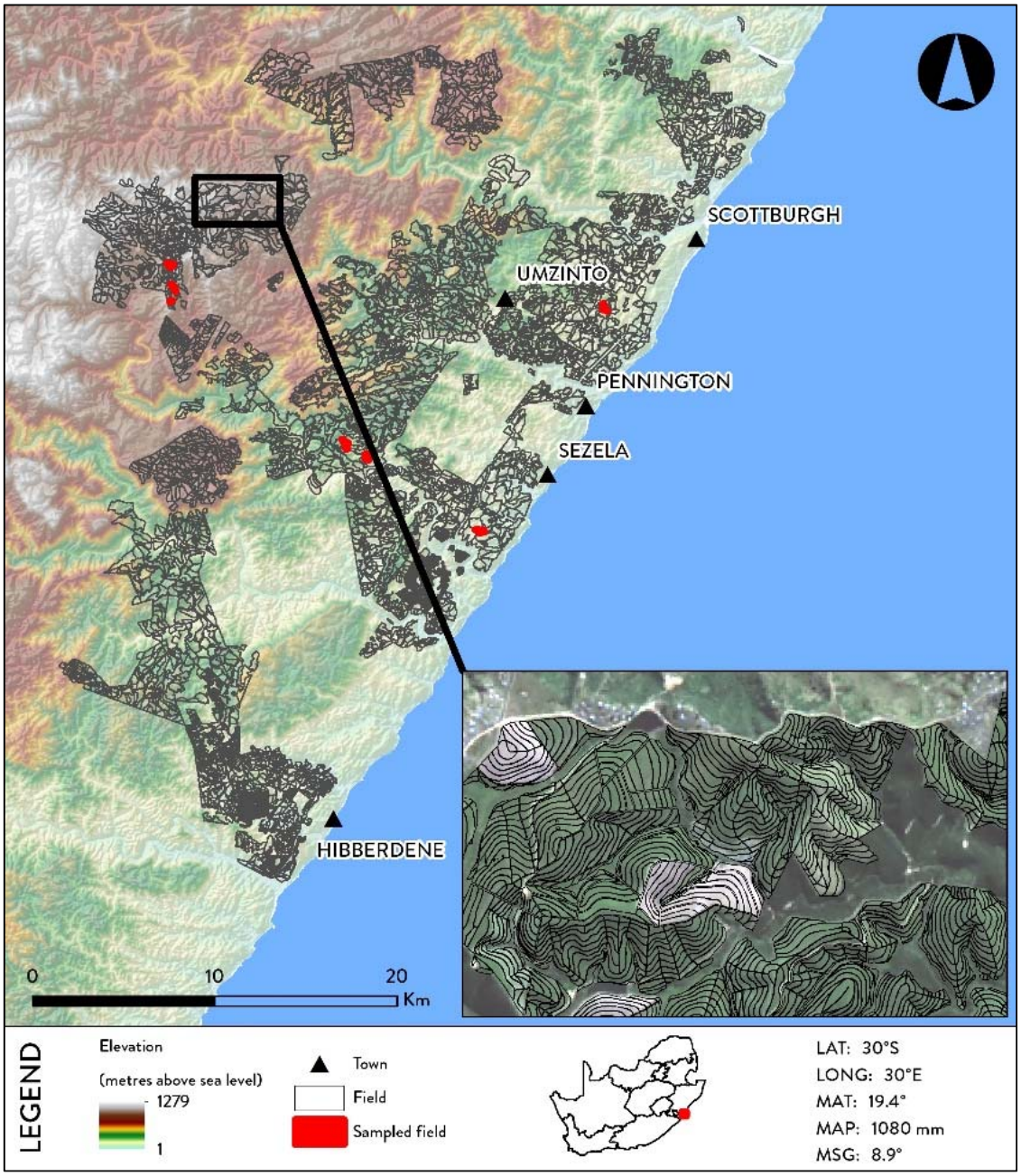

Figure 2 Sezela study area with an example of its typical 'contour like' field structure, resulting in narrow, elongated fields

2.2 Data acquisition and preparation

2.2.1 In situ fAPAR measurements

Twenty fields were selected, ten in each of the two study areas. Fields were selected to get as good a representation as possible of the different topography, soil, climate and management conditions prevailing in each area. Management aspects included cultivar, row spacing and configuration, growing period and time of harvest, harvesting method (green or burnt cane), and irrigation system. Selected fields also included different levels of management quality.

fAPAR was estimated by measuring incident (above the crop canopy) and transmitted (below the lowest green leaf) photosynthetically active radiation (INPAR and TPAR respectively) with a portable line quantum sensor (Model AccuPar LP80, Decagon Devices, Pullman, USA) at approximately monthly intervals at five positions in each of the validation fields (Supplementary Material 1) (Figure 1 and Figure 2 for Pongola and Sezela respectively). Coordinates of measurement positions were recorded using a handheld Trimble® Juno® 3B global navigation satellite system (Trimble Navigation Limited, Westminster, USA) with a post processing accuracy of 1 to 3 m. Each measurement was taken between 11h00 and 13h00 on cloud free days and consisted of ten readings, evenly distributed within a marked 5m section along two adjacent cane rows, taken below the bottom most green leaf, and one reading above the canopy. Dates of the field measurements are summarized in Supplementary Material 2. The fAPAR by the green canopy was calculated as:

$$fAPAR = 1 - \frac{\frac{1}{n}\sum TPAR}{INPAR} \qquad \text{Equation 1}$$

Where	fAPAR	is the estimated fraction of incoming PAR intercepted by the green canopy;
	TPAR	represents the measured transmitted PAR;
	INPAR	represents the measured incident PAR; and
	n	is the number of TPAR readings.

Equation 1 assumes that reflection of PAR from soil and leaves are negligible. According to the manual of the quantum sensor it can be assumed that F ≈ 1 – T and that the error because of this assumption would be smaller than 0.05. In this study fAPAR values were converted to a percentage by multiplying the 0 to 1 fraction by 100. Landsat-8 data collection and preparation

A total of 38 Landsat-8 Operational Land Imager (OLI) images were acquired from the United States Geological Survey (USGS) for the same time period as the in situ data collection (Supplementary Material 3). Landsat-8 is a sun-synchronous, moderate resolution satellite with a revisit time of 16 days. The OLI sensor has eight spectral bands with a spatial resolution of 30m, and a panchromatic band with a spatial resolution of 15m (Supplementary Material 4). Each acquired image was atmospherically corrected and converted from digital numbers to percentage surface reflectance using the ATCOR-2 algorithm (version 8.3) (Richter, 2004). Given the demonstrated benefits of pan-sharpening Landsat-8 imagery for crop monitoring (Gilbertson et al., 2017), the resolution of all multispectral bands were increased to 15 m using the statistical Pansharp algorithm as implemented in PCI Geomatica, 2016 (Nikolakopoulos, 2008; Zhang, 2002).

The pre-processed images were manually inspected for cloud cover. Images on which sampling sites were influenced by clouds or cloud shadow (seven cases in total) were omitted from further analysis (Supplementary Material 3).

The surface reflection values (all bands) of the retained images were extracted for each sampling site. In situ observations were matched to the image dates as closely as possible. The average offset between in situ observations and image acquisition dates was 5 days, with a maximum offset of 14 days.

Several transformations were implemented to increase the dimensionality of the variable dataset and to model the vigour and moisture properties of sugarcane. Vegetation indices (VIs) are common image transformations and are based on the band rationing principle that exploits the contrast between healthy vegetation's absorption of electromagnetic (EM) radiation in the visible spectrum and its high reflectance of EM radiation in the NIR region. VIs considered for the modelling of fAPAR are summarized in **Table 1**.

Table 1 VIs considered for modelling fAPAR.

Index	Equation	Reference
1. Simple ratio (SR)	$SR = Band5/Band4$	(Jordan, 1969)
2. Normalized difference vegetation index (NDVI)	$NDVI = (Band5 - Band4)/(Band5 + Band4)$	(Rouse, 1973)
3. Green normalized difference vegetation index (GNDVI)	$GNDVI = (Band5 - Band3)/(Band5 + Band3)$	(Gitelson et al., 1996)
4. Soil adjusted vegetation index (SAVI)	$SAVI = (1 + 0.5)(Band5 - Band4)/(Band5 + Band4 + 0.5)$	(A.R. Huete, 1988)
5. Enhanced vegetation index (EVI)	$EVI = 2.5(\frac{Band5 - Band4}{Band5 + 6Band4 + 7.5Band2 + 1})$	(Huete et al., 1996)
6. Modified triangular vegetation index ($MTVI^2$)	$MTVI^2 = \frac{1.5(1.2(Band5 - Band3) - 2.5(Band4 - Band3))}{\sqrt{(2Band5 + 1)^2 - (6Band5 - 5\sqrt{Band4}) - 0.5}}$	(Haboudane et al., 2004)
7. Normalized difference moisture? index ($NDMI\text{-}SWIR^1$)	$NDMI\ SWIR^1 = (Band5 - Band7)/(Band5 + Band7)$	(Gao, 1996)
8. $NDMI\text{-}SWIR^2$	$NDMI\ SWIR^2 = (Band5 - Band8)/(Band5 + Band8)$	(Gao, 1996)
9. Aerosol free vegetation index, $SWIR^1$ ($AFRI\text{-}SWIR^1$)	$AFRI\ SWIR^1 = (Band5 - 0.66Band7)/(Band5 + 0.66Band7)$	(Karnieli et al., 2001)
10. $AFRI\text{-}SWIR^2$	$AFRI\ SWIR^2 = (Band5 - 0.5Band8)/(Band5 + 0.5Band8)$	(Karnieli et al., 2001)

The SR (**Table 1**a) was first used by Jordan (1969) to measure LAI of a forest canopy. The SR is based on the principal that leaves absorb light at 675 nm and reflects light at 800 nm, which means that an increase in leaves would result in an increase of the SR. Rouse (1973) elaborated on this ratio by computing the normalized difference thereof, resulting in the NDVI (**Table 1**b), which is one of the most commonly employed VIs in remote sensing. The NDVI has been shown to have a number of limitations, which led to various adaptations. Gitelson et al. (1996) introduced the GNDVI (**Table 1**c) and found that it was at least five times more sensitive to chlorophyll concentrations in plant leaves than NDVI, which

would saturate at high chlorophyll levels. Huete (1988) proposed the SAVI (**Table 1**d) to reduce NDVI's sensitivity to soil background brightness (Bausch, 1993). The SAVI introduces a soil adjustment factor to counter the effect of soil brightness. This factor can vary from 0 to 1 depending on the amount of visible soil. Higher values ought to be used in areas with greater proportions of visible bare soil. The EVI (**Table 1**e) was developed as part of the Moderate Resolution Imaging Spectroradiometer (MODIS) mission to be more sensitive to high vegetation densities while reducing atmospheric influences (Jiang et al., 2008). The $MTVI^2$ (**Table 1**f) was specifically developed for estimating the LAI and incorporates a higher sensitivity to chlorophyll levels and a reduction in soil background noise.

Karnieli et al. (2001) showed that SWIR reflectance in the 1.6 and 2.1 µm region are highly correlated with visible blue, green and red spectral reflectance under clear sky conditions. Cloud therefore indirectly represent a fAPAR component. Furthermore, the SWIR region of the EM spectrum is known for its sensitivity for soil and vegetation moisture content (Chuvieco and Huete, 2010). The normalized difference wetness index (NDWI) was introduced by Gao (1996) and combines the NIR band (centralized at around 0.86 µm) and the SWIR band (centralized around 1.24 µm) in a normalized difference ratio. According to Ceccato et al (2001), the equivalent water thickness (ETW) concept can be used to successfully estimate vegetation water content. They proposed the global vegetation moisture index (GVMI), which is a normalized difference ratio between the NIR and SWIR bands with coefficients to reduce geophysical and atmospheric effects. This approach is often called the normalized difference moisture index (NDMI) (Jin and Sader, 2005) or the shortwave infrared water stress index (SIWSI) (Fensholt and Sandholt, 2003). The nomenclature of these indices vary, but in this study we implemented two moisture indices, namely $NDMI\text{-}SWIR^1$ (**Table 1**g) and $NDMI\text{-}SWIR^2$ (**Table 1**h). The aerosol free vegetation index (AFRI) (Karnieli et al., 2001) is known for its ability to perform well under atmospheric conditions such as smoke plumes caused by fires and when certain sulphates are present (Ben-Zeev et al., 2006). Although AFRI is less popular compared to the VIs discussed above, it was included in this study because pre-harvest burning is a common occurrence in South African sugarcane fields. Two versions of AFRI, namely $AFRI\text{-}SWIR^1$ (**Table 1**i) and $AFRI\text{-}SWIR^2$ (**Table 1**j), were implemented to exploit both shortwave infrared (SWIR) bands of the OLI sensor. All the indices described in **Table 1** were used in combination with the individual reflectance bands 4, 5, 7 and 8 (Supplementary Material 4) to assess their suitability for modelling sugarcane fAPAR in the study areas.

2.3 Experimental design

2.3.1 Unit of analysis

The experiments were carried out within the geographical object-based image analysis (GEOBIA) paradigm, with each object representing an individual sugarcane field. The motivation for not using a pixel-based approach was that most crop growth models (e.g. CANESIM) operate at field level. Also, an object-based approach was considered less susceptible to within-field variations in fAPAR, uncertainties in the positional accuracy of the in situ measurements (~ 5m), and possible geometrical offsets (~ 15m) in the imagery. A GIS database of fields, digitized from high-resolution aerial photographs, was consequently used as the unit of analysis.

The fAPAR in situ measurements were aggregated per field to produce a single value (Figure 3), resulting in 69 and 57 mean fAPAR values for Pongola and Sezela respectively. Reflectance values were similarly averaged for each field using the zonal statistic algorithm as implemented in ArcMap (version 10.4). To minimize the effect of mixed pixels caused by adjacent features located at the edges of fields (e.g. roads or bare fields), only pixels that were 15 m or further away of field edges were considered (Figure 3). Mean reflectance and index values were extracted within the retained areas.

The experiments were carried out on three different groups of data to evaluate the differences in modelling fAPAR for the two diverse study areas. The first two groups of experiments targeted the two individual areas (69 fields in Pongola and 57 fields in Sezela), while a third group of experiments were carried out on two study area combined (126 fields in Combined).

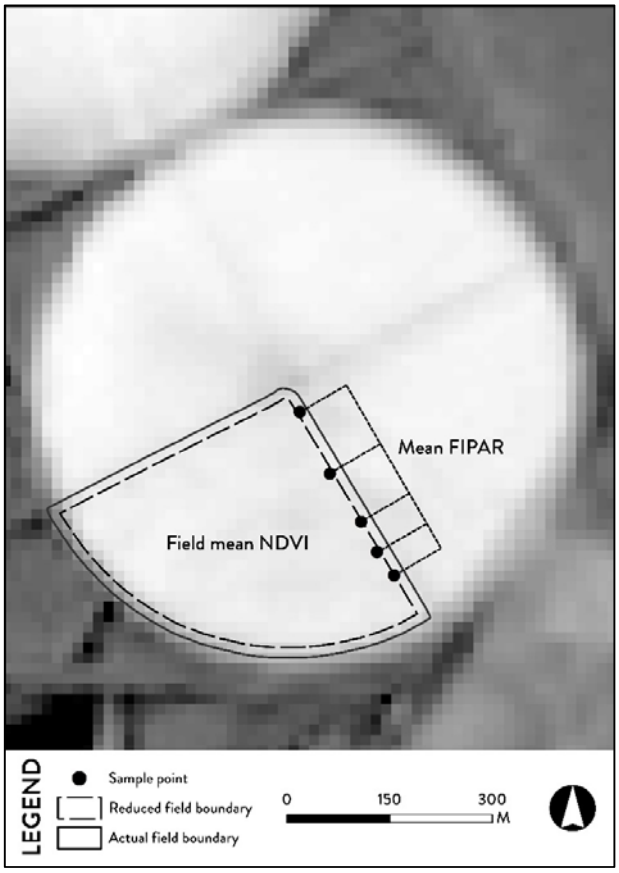

Figure 3 Conceptual overview of in situ measurement aggregation and reflectance extractions

2.3.2 Statistical analyses

The mean reflectance and index values of all 126 sampled fields (from both study areas) were used as input to a bivariate correlation analysis to investigate the collinearity among variables. This was followed by a series of univariate regression analyses. **Table 2** lists the regression models that were considered in the model building process. In all cases, the aggregated fAPAR measurements were set as the dependent variable, while the individual image variables were used as independent variables.

Table 2 Regression models considered for analysis

Variable Type	Regression model	Definition
Single	Linear	$y = mx + c$
	Quadratic	$y = m_1x + m_2x^2 + c$
	Cubic	$y = m_1x + m_2x^2 + m_3x^3 + c$
Multi	Decision tree (DT) regressor	As described in Breiman et al. (1984)
	Random Forest (RF) regressor	As described in Breiman, (2001)

y = dependant variable; x = independent variable; mn = slope/coefficient; c = constant/intercept

Each regression model was cross-validated using bootstrapping with 1500 iterations (Wilcox, 2001) to reduce the effect of outliers and to normalize the results. During each iteration the fAPAR measurements were randomly subdivided into an independent training (70%) and test (30%) sample. The test samples were used to calculate a root mean squared error (RMSE) for the predicted fAPAR values. The reported results of each regression model is therefore an average of the model's "goodness of fit" (R^2) and the model's performance (RMSE) throughout the 1500 iterations.

The by-products of the bootstrapping exercise were populations of R^2, RMSE and regression model coefficient values (slope and intercept values (Table 2)) which enabled a statistical analysis on whether there were significant differences between relevant population means. The one-way ANOVA test was used to determine whether the difference between normally distributed populations (populations where tested for normality using D'Agostino and Pearson, (1973)'s algorithm) was statistically significant. The non-parametric Wilcoxon singed-rank test was used for skewed populations.

Two machine learning algorithms were considered for modelling fAPAR. Given that the ultimate application of fAPAR will be for forcing a CGM, a continuous (as opposed to categorical) quantification was required. Decision tree (DT) and random forest (RF) regressors were consequently implemented. The DT regressor was trained with an unlimited tree depth (no pruning) and all variables were considered to find the best split (active variables). The RF regressor was trained with a default number of ten trees per forest, the number of active variables was set equal to all image variables, and the tree depth was set to unlimited (no pruning). The mean squared error (MSE) was used as quality measuring criterion for each split in the DT and RF models.

To further compare the impact of sugarcane variety, different geographical and environmental conditions and farming practice, the sugarcane fAPAR models proposed by Morel et al. (2014) (fAPAR = 1.3829NDVI – 0.3333) and Zhang et al. (2015) (fAPAR = 1.312NDVI – 0.1921), as well as a generic fAPAR model derived by Bastiaanssen and Ali (2003) (fAPAR = 1.257NDVI -0.161) were implemented in the bootstrapping exercise. The latter model was developed based on empirical corn, soybean (Daughtry et al., 1992) and sunflower (Joel et al., 1997) data, combined with a radiative transfer model (Myneni, 1997).

All statistical analyses were automated in Python (version 2.7.12) using the open source SciPy (Oliphant, 2007) and Scikit-learn (Pedregosa et al., 2012) statistical libraries.

3 RESULTS

The progression of fAPAR estimates over time are shown for four example fields (**Error! Reference source not found.**). The remotely sensed fAPAR estimates generally agreed well with in situ measurements. Field P5 shows a rapid increase in fAPAR from June to November 2015, a slight decline thereafter with subsequent recovery from January 2016 onwards. Field P9 shows an initial increase up to September 2015, then a steady decline up to February 2016, coinciding with a period of water stress, and then a recovery in March and April of 2016. These contrasting patterns of development are explained by the irrigation water supply that became severely restricted from October 2015. Farmers implemented different coping strategies. For instance, Field P5 was prioritized over other fields on the farm with lower yield potentials, while field P9 bared the brunt of the restricted water supply.

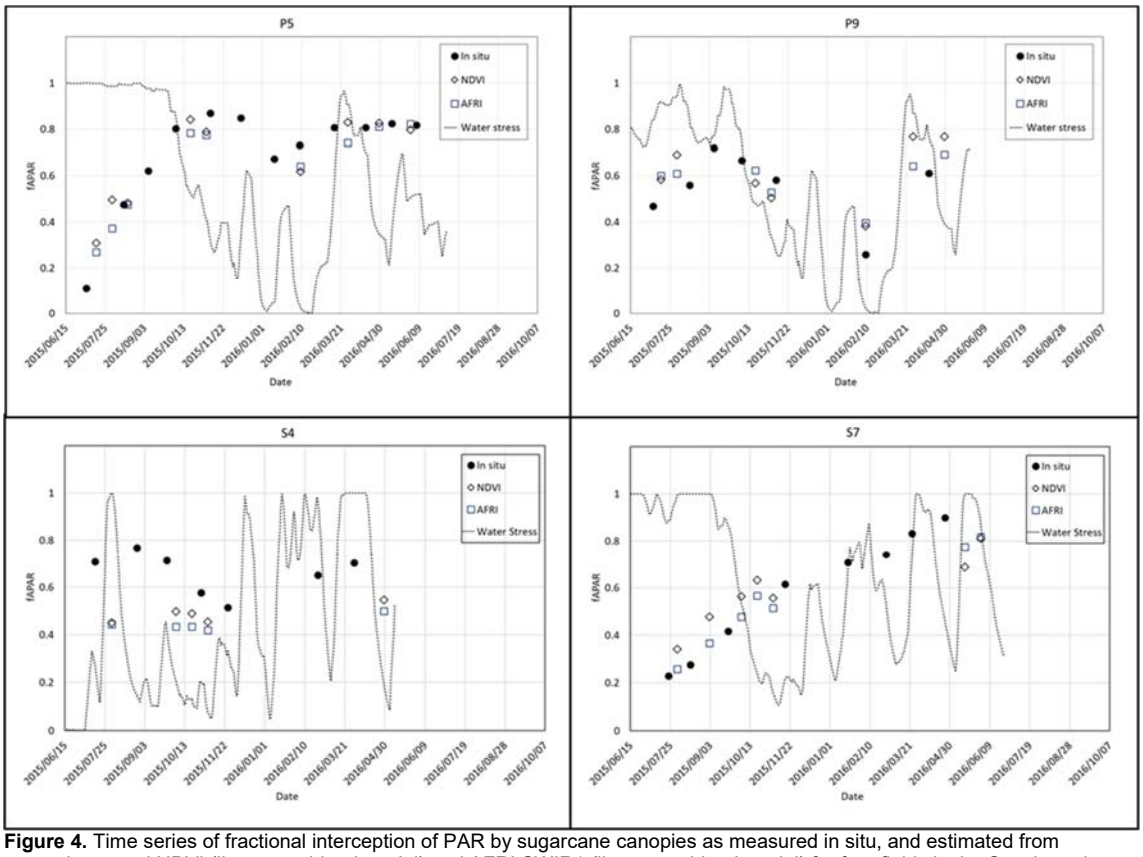

Figure 4. Time series of fractional interception of PAR by sugarcane canopies as measured in situ, and estimated from remotely sensed NDVI (linear combined model) and AFRI SWIR1 (linear combined model) for four fields in the Sezela and Pongola mill supply areas. An index of regional water stress (1 - no stress, 0 - severe stress) is also shown as simulated by the Canesim Crop Forecasting System (Bezuidenhout & Singels, 2007).

At Sezela, Field S4 shows declining in situ measured fAPAR in 2015 during a time of severe water stress, and partial recovery in 2016. Remote sensing estimates are higher than in situ measurements of fAPAR in 2016. Field S7 shows a steady increase in fAPAR as the crop canopy developed, with good agreement between remote sensing estimates and in situ measurements.

3.1 Bivariate correlation

The bivariate correlation yielded the Pearson's correlation statistics (R) and the p significance values as shown in Table 3. From these results it is clear that many of the independent variables are highly correlated. For instance, most of the VIs (excluding the SR) have R statistics of more than 0.92. Due to the high redundancy among variables, it was assumed that the regression modelling outputs would be similarly correlated. A high level of statistical significance of the ANOVA and Wilcoxon tests would consequently be required to reject the null hypothesis that the variables provide similar information. Therefore, an alpha level of $p < 0.001$ was used for establishing the statistical significance.

Table 3 Bivariate correlation (Pearson R statistic) between variables considered for model building.

	Band 4	Band 5	Band 7	Band 8	SR	NDVI	GNDVI	SAVI	EVI	MTVI^2	NDMI SWIR^1	NDMI SWIR^2	AFRI SWIR^1	AFRI SWIR^2
Band 4	1*	-0.42*	0.88*	0.86*	-0.74*	-0.76*	-0.72*	-0.76*	-0.74*	-0.74*	-0.73*	-0.68*	-0.71*	-0.65*
Band 5	-0.42*	1*	-0.21	-0.58*	0.77*	0.88*	0.87*	0.88*	0.8*	0.84*	0.88*	0.89*	0.87*	0.88*
Band 7	0.88*	-0.21	1*	0.89*	-0.58*	-0.56*	-0.51*	-0.55*	-0.59*	-0.54*	-0.62*	-0.57*	-0.61*	-0.55*
Band 8	0.86*	-0.58*	0.89*	1*	-0.76*	-0.82*	-0.78*	-0.82*	-0.83*	-0.82*	-0.88*	-0.87*	-0.88*	-0.86*
SR	-0.74*	0.77*	-0.58*	-0.76*	1*	0.88*	0.9*	0.88*	0.81*	0.82*	0.88*	0.85*	0.86*	0.82*
NDVI	-0.76*	0.88*	-0.56*	-0.82*	0.88*	1*	0.97*	1*	0.94*	0.98*	0.97*	0.97*	0.97*	0.96*
GNDVI	-0.72*	0.87*	-0.51*	-0.78*	0.9*	0.97*	1*	0.98*	0.89*	0.94*	0.94*	0.94*	0.94*	0.93*
SAVI	-0.76*	0.88*	-0.55*	-0.82*	0.88*	1*	0.98*	1*	0.94*	0.98*	0.97*	0.97*	0.97*	0.96*
EVI	-0.74*	0.8*	-0.59*	-0.83*	0.81*	0.94*	0.89*	0.94*	1*	0.94*	0.93*	0.93*	0.93*	0.92*
MTVI^2	-0.74*	0.84*	-0.54*	-0.82*	0.82*	0.98*	0.94*	0.98*	0.94*	1*	0.94*	0.95*	0.95*	0.95*
NDMI-SWIR^1	-0.73*	0.88*	-0.62*	-0.88*	0.88*	0.97*	0.94*	0.97*	0.93*	0.94*	1*	0.99*	1*	0.98*
NDMI-SWIR^2	-0.68*	0.89*	-0.57*	-0.87*	0.85*	0.97*	0.94*	0.97*	0.93*	0.95*	0.99*	1*	0.99*	1*
AFRI-SWIR^1	-0.71*	0.87*	-0.61*	-0.88*	0.86*	0.97*	0.94*	0.97*	0.93*	0.95*	1*	0.99*	1*	0.99*
AFRI-SWIR^2	-0.65*	0.88*	-0.55*	-0.86*	0.82*	0.96*	0.93*	0.96*	0.92*	0.95*	0.98*	1*	0.99*	1*

* $p < 0.001$

3.2 Univariate regression

Table 4 summarizes the performance of the fAPAR models that relied on individual image variables. In the interest of brevity, only the five best modelling results for each set of experiments (per region and both regions combined) and per regression model (linear, quadratic and cubic) are included (NDVI is listed in all areas for comparison purposes). It is evident that the cubic regression models generally outperformed the linear and quadratic models. For instance, the strongest models (R^2=0.957, RMSE=7.72) were achieved in Pongola when SAVI was used as input to a cubic model. In the Pongola region, SAVI achieved slightly higher accuracies than NDVI, suggesting that SAVI reduced some of the effects of soil background reflectance. The differences in the RMSE populations between SAVI and NDVI were, however, not statistically significant in this region ($F<1.4$; $p>0.24$).

The difference in RMSE populations (produced from the iterations) between the best performing SWIR-based indices and SAVI in the Pongola region was statistically significant for the linear (NDMI-SWIR^1) and quadratic (AFRI-SWIR^1) models ($F=39$, $p<0.001$; and $F=17$, $p<0.001$ respectively), but was not significant for the cubic model ($T=1.3$; $p=0.25$).

Table 4 fAPAR regression modelling results based on individual image variables, where x̄ refers to the mean and σ refers to the standard deviation value of the specified (R^2 or RMSE) population.

	Linear				Quadratic				Cubic			
Region	Image variable	R^2		RMSE		Image variable	R^2		RMSE		Image variable	R^2		RMSE	
		x̄	σ	x̄	σ		x̄	σ	x̄	σ		x̄	σ	x̄	σ
Pongola	1) SAVI	0.945	0.01	8.35	1.02	1) SAVI	0.947	0.01	8.41	1.09	1) SAVI	0.957	0.01	7.72	1.04
	2) NDVI	0.944	0.01	8.39	1.03	2) NDVI	0.946	0.01	8.45	1.10	2) NDVI	0.956	0.01	7.76	1.04
	3) NDMI-SWIR^1	0.942	0.01	8.59	1.10	3) MTVI^2	0.946	0.01	8.51	1.23	3) AFRI-SWIR^1	0.956	0.01	7.77	1.22
	4) AFRI-SWIR^1	0.935	0.01	9.12	1.16	4) AFRI-SWIR^1	0.946	0.01	8.58	1.21	4) NDMI-SWIR^1	0.954	0.01	8.02	1.24
	5) NDMI-SWIR^2	0.924	0.01	9.87	1.30	5) NDMI-SWIR^1	0.944	0.01	8.70	1.19	5) SR	0.953	0.01	8.29	1.40
Sezela	1) NDMI-SWIR^1	0.834	0.03	13.9	2.06	1) SWIR^2	0.867	0.02	13.0	1.84	1) SWIR^2	0.885	0.02	12.6	2.26
	2) AFRI-SWIR^1	0.833	0.03	14.0	1.97	2) AFRI-SWIR^2	0.85	0.03	13.6	2.18	2) NDMI-SWIR^2	0.877	0.02	12.7	2.27
	3) NDMI-SWIR^2	0.833	0.03	14.0	1.94	3) NDMI-SWIR^2	0.843	0.03	14.0	2.14	3) AFRI-SWIR^1	0.866	0.03	13.1	2.38
	4) AFRI-SWIR^2	0.815	0.03	14.9	1.97	4) AFRI-SWIR^1	0.837	0.03	14.2	2.13	4) NDMI-SWIR^1	0.864	0.03	13.1	2.40
	5) SWIR^2	0.809	0.02	15.3	1.82	5) NDMI-SWIR^1	0.837	0.03	14.3	2.10	5) AFRI-SWIR^2	0.872	0.02	13.3	2.45
	7) NDVI	0.753	0.04	16.9	2.28	7) NDVI	0.755	0.04	17.28	2.39	7) NDVI	0.769	0.04	16.85	2.64
Pongola & Sezela combined	1) NDMI-SWIR^1	0.892	0.01	11.3	1.27	1) AFRI-SWIR^2	0.898	0.01	11.1	1.35	1) NDMI-SWIR^2	0.911	0.01	10.4	1.43
	2) AFRI-SWIR^1	0.889	0.01	11.5	1.20	2) AFRI-SWIR^1	0.894	0.01	11.3	1.32	2) AFRI-SWIR^1	0.912	0.01	10.4	1.42
	3) NDMI-SWIR^2	0.882	0.01	11.8	1.26	3) NDMI-SWIR^1	0.893	0.01	11.4	1.29	3) AFRI-SWIR^2	0.91	0.01	10.5	1.39
	4) AFRI-SWIR^2	0.863	0.01	12.8	1.33	4) NDMI-SWIR^2	0.892	0.01	11.4	1.33	4) NDMI-SWIR^1	0.909	0.01	10.6	1.44
	5) NDVI	0.861	0.02	12.8	1.52	5) MTVI^2	0.878	0.01	12.1	1.37	5) MTVI^2	0.885	0.01	11.8	1.45
	-	-	-	-	-	6) NDVI	0.862	0.02	13.0	1.55	6) NDVI	0.874	0.02	12.4	1.74

Generally, the Sezela models were much weaker compared to those of Pongola. Specifically, the NDVI-SAVI models performed relatively poorly in Sezela, with the best performing models being dominated by the SWIR bands and/or indices. For example, the cubic model achieved an R^2=0.885 and RMSE=12.7 when the untransformed $SWIR^2$ band was used. All the SWIR based VIs performed significantly better (linear F=955; quadratic F=1408; and cubic F=988 with $p<0.001$) than the best performing non-SWIR VIs ($MTVI^2$ in all cases). It is clear from the difference in magnitude of the ANOVA-F values that the variation between the SWIR-based and non-SWIR-based indices are much more pronounced in Sezela (compared to Pongola).

The results of the third set of experiments (performed on the combined fields of the Pongola and Sezela regions) similarly showed that the SWIR-based indices outperformed the non-SWIR-based indices. Even though the number of fields sampled in the Pongola were more than in Sezela (69:57 ratio), the magnitude of the differences between the SWIR-based and non-SWIR-based indices in Sezela (maximum F value 1408, compared to 39 in Pongola) resulted in the SWIR-based indices dominating when the fields of two regions were combined. The cubic NDMI-$SWIR^2$ model (R^2=0.911, RMSE=10.4) was significantly different (Wilcoxon T=34K; $p<0.001$) than the best-performing non-SWIR based VI, namely $MTVI^2$ (R^2=0.885, RMSE=11.8). The same trend was observed for the quadratic AFRI-$SWIR^2$ model against $MTVI^2$ (F=421; $p<0.001$); and the linear NDMI-$SWIR^1$ model against NDVI (F=962; $p<0.001$).

Figure 4 illustrates the relationship between in situ fAPAR measurements and two VIs, NDVI and NDMI-$SWIR^1$, for the three sets of experiments. The relationships between the in situ fAPAR measurements and the VIs are near-linear, although the cubic model produced lower RMSEs. The difference between the linear and cubic RMSE populations where significant for all three sets of experiments. The cubic models should, however, be interpreted with caution, since it is susceptible to overfitting. For example, the fAPAR values of the cubic NDMI-$SWIR^1$ model in Sezela (Figure 4) start to decrease at values of greater than 0.4, which is unlikely in reality. Regression coefficient values (e.g. slope and intercept values) between comparable regression models within each of the three sets of experiments (e.g. linear NDVI model for Pongola, Sezela and combined fields) showed significant differences for all variables in all cases.

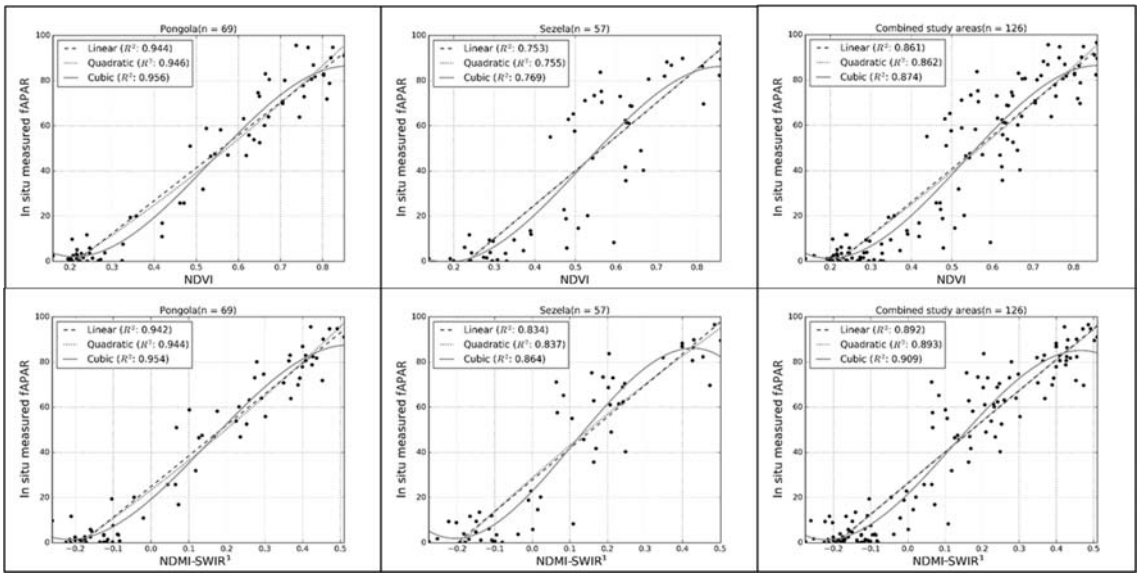

Figure 4 Empirical fAPAR models based on NDVI and NDMI-SWIR[1] for Pongola, Sezela and combined regions.

3.3 Multi-variate regression

The results of the DT and RF multivariate regression analyses are summarized in Table 5 and Table 6. RF regression consistently outperformed DT in all experiments ($p < 0.001$) with the lowest mean RMSE (8.439) recorded in the Pongola region. Despite this relatively low error, the multivariate machine learning models were unable to outperform the NDVI/SAVI univariate regression models in Pongola (compare Table 4), while in Sezela the RF univariate model produced significantly lower ($p < 0.001$) error levels (RMSE=11.9%) compared to the best univariate model (RMSE=12.7%). The NDMI-SWIR[2] univariate model (RMSE=10.4%) also produced significantly better results than DT (RMSE=13.7%) and RF (RMSE=10.8%) when the study areas were combined.

Table 5 Results of the multivariable decision tree (DT) and random forest (RF) regression models for Pongola, Sezela and the two areas combined where $\bar{x}$ refers to the mean and σ refers to the standard deviation value of the RMSE population.

	DT		RF	
	RMSE		RMSE	
	$\bar{x}$	σ	$\bar{x}$	σ
Pongola	10.46	1.92	8.54	1.49
Sezela	14.32	3.89	11.86	2.68
Pongola & Sezela combined	13.67	2.19	10.72	1.71

The main purpose of implementing DT and RF was to gain additional insight into the importance of individual independent variables (Table 6). NDVI and SAVI dominated in Pongola, while the SWIR[2] band and SWIR-based NDMI and AFRI indices were the most important variables in Sezela. The SWIR-based NDMI and AFRI indices were also the most important variables when the areas were combined.

Table 6 The mean percentage variable importance (%VI) of the multi variable regression analyses, where IMV refers to the image variable and σ refers to the standard deviation (%)

Pongola						Sezela						Pongola & Sezela combined					
DT			RF			DT			RF			DT			RF		
IMV	% VI	σ	IMV	% VI	σ	IMV	% VI	σ	IMV	% VI	σ	IMV	% VI	Σ	IMV	% VI	σ
SAVI	19	35	NDVI	14	10	$SWIR^2$	65	39	$SWIR^2$	40	21	AFRI $SWIR^2$	16	31	$SWIR^2$	18	16
NDVI	19	35	SR	13	9.7	AFRI $SWIR^2$	6.3	22	NDMI $SWIR^2$	10	9.3	NDMI $SWIR^1$	16	32	AFRI $SWIR^1$	15	12
SR	18	35	SAVI	13	9.6	NDMI $SWIR^2$	6.1	21	AFRI $SWIR^2$	9.9	9.2	AFRI $SWIR^1$	16	31	NDMI $SWIR^1$	15	12
$MTVI^2$	17	34	$MTVI^2$	13	10	AFRI $SWIR^1$	5.5	21	AFRI $SWIR^1$	8.2	8.9	$SWIR^2$	15	29	AFRI $SWIR^2$	13	11
AFRI $SWIR^1$	6.3	21	NIR	8.9	11	NDMI $SWIR^1$	5.1	20	NDMI $SWIR^1$	8.0	8.5	NDMI $SWIR^2$	15	31	NDMI $SWIR^2$	12	11
NDMI $SWIR^1$	5.3	19	AFRI $SWIR^1$	8.2	8.3	EVI	3.1	3.5	Red	4.6	7.1	SR	6.8	21	SR	7.4	9.0
NIR	5.0	18	NDMI $SWIR^1$	8.2	8.1	Red	2.0	11	$SWIR^1$	4.6	6.6	$MTVI^2$	5.6	19	$MTVI^2$	6.0	7.5
AFRI $SWIR^2$	3.1	11	GNDVI	5.5	6.4	SR	1.4	5.7	EVI	3.1	3.0	SAVI	2.8	13	NDVI	3.9	6.0
GNDVI	2.0	11	AFRI $SWIR^2$	4.9	5.9	$MTVI^2$	1.1	6.4	$MTVI^2$	3.1	5.0	NDVI	2.6	13	SAVI	3.6	5.6
EVI	2.0	10	NDMI $SWIR^2$	4.6	5.9	GNDVI	1.0	2.8	SR	2.6	4.2	GNDVI	1.3	3.5	GNDVI	1.9	2.8

This finding corresponds very well with the univariate regression modelling results (Table 4), where NDVI and SAVI performed well in Pongola, but poorly in Sezela. These variable importance lists should, however, be interpreted with caution as many of the “best” variables are highly correlated and thus redundant. For instance, NDVI and SAVI are highly correlated (R = 1, Table 3) and the exclusion of either will most likely not have had a significant effect on performance of the models.

3.4 mparison to existing models

The resulting RMSE values of the sugarcane fAPAR models of Morel et al. (2014), Zhang et al. (2015) and Bastiaanssen and Ali (2003) are reported in Table 7, along with a summary of the NDVI and best-performing models developed in this study (taken from Table 4). In all cases, the NDVI-based and best-performing linear, quadratic and cubic models generated in this study were significantly ($p < 0.001$) stronger than those of previous studies.

Table 7 RMSE values and model coefficients for fAPAR models of Morel et al. (2014), Zhang et al. (2015) and Bastiaanssen and Ali (2003) compared to the models derived in this study. Where Y represents the model’s intercept and X represents the model’s slope/s, IMV represents the image variable, and BP represents the best performing image variable.

		Pongola			Sezela			Combined Sezela & Pongola		
Model	**IMV**	**RMSE**	**Y***	**X***	**RMSE**	**Y***	**X***	**RMSE**	**Y***	**X***
Linear (Morel)	NDVI	9.88	- 0.3333	1.3829	17.15	- 0.3333	1.3829	13.70	- 0.3333	1.3829
Linear (Zhang)	NDVI	10.16	- 0.1921	1.312	17.90	- 0.1921	1.312	14.30	- 0.1921	1.312
Linear (Bastiaanssen)	NDVI	10.85	- 0.161	1.257	18.28	- 0.161	1.257	14.70	- 0.161	1.257
Linear (this study)	BP	8.35[1]	-0.30754	0.9755	13.95[4]	0.2779	1.3945	11.26[7]	0.2629	1.3710
	NDVI	8.39	-0.31156	1.4507	16.93	-0.3501	1.5005	12.85	-0.3255	1.4672
Quadratic (this study)	BP	8.41[2]	-0.23194	x: 0.7062 x^2: 0.186	12.99[5]	1.4597	x: -0.1043 x^2: 0.00019	11.08[8]	-0.0179	x: -0.1844 x^2: 1.4945
	NDVI	8.45	-0.23249	x: 1.0353 x^2: 0.4247	17.27	-0.347	x: 1.4805 x^2: 0.0239	12.95	-0.2769	x: 1.2240 x^2:0.2467
Cubic (this study)	BP	7.72[3]	0.333	x: -2.209 x^2: 4.452 x^2: -1.877	12.56[6]	1.023	x: -0.00001 x^2: -0.0053 x^2: 0.00014	10.39[9]	0.0469	x: 0.5778 x^2: 2.5103 x^2: -2.4335
	NDVI	7.76	0.347	x: -3.373 x^2: 9.961 x^3: -6.209	16.84	0.221	x: -2.6433 x^2: 8.7493 x^3: -5.5895	12.40	0.2868	x: -2.9992 x^2:9.3231 x^3:-5.8777
DT (this study)	All	10.46	-	-	14.32	-	-	13.67	-	-
RF (this study)	All	8.54	-	-	11.86	-	-	10.72	-	-
Overall mean		8.996	-	-	15.46	-	-	12.55	-	-

[1,2,3] SAVI, [4] NDMI-SWIR[1], [5,6] SWIR[2], [7] NDMI-SWIR[1], [8] AFRI-SWIR[2], [9] NDMI-SWIR[2]

* model output fAPAR fractions can be multiplied by 100 to provide % fAPAR values.

4 DISCUSSION

The potential of remotely sensed imagery for modelling sugarcane fAPAR has been demonstrated in several previous studies. However, previous studies evaluated the developed models in areas where the cropping and environmental conditions were relatively homogenous. In this study, three existing and a number of new sugarcane fAPAR models were implemented in two contrasting areas to better

understand model robustness. It was found that cropping and environmental conditions were the main drivers of sugarcane fAPAR modelling success. Significantly (40%) lower mean RMSE values were recorded in Pongola, which is attributed to the relatively homogenous conditions under which sugarcane is grown in this area. Specifically, the sugarcane in this area is irrigated, which means that the likelihood of water stress is lower compared to the rainfed cropping practiced in Sezela. The effect of this is that the canopy cover in Pongola is more uniform (homogenous, less variation in LAD), resulting in the in situ fAPAR samples being less variable and more representative of the within-field conditions. The climate and landscape of Sezela is also much more diverse, with the coastal regions being warm and wet and the inland areas experiencing cooler and dryer conditions. It is also conceivable that atmospheric influences were more pronounced in Sezela, which is located along the coast with larger sources of aerosols (e.g. larger urban populations and industries), which could have contributed to the relatively poor results in this region. It is likely that topography also contributed to the relatively poor performance of the models in Sezela, given that the landscape in Pongola is relatively flat and homogenous (mean slope gradient of 2.5°, standard deviation of 1.5°) compared to Sezela's undulating terrain (mean slope gradient of 8.9°, standard deviation of 5°). These topographical variations are known to affect local climate, with north-facing slopes generally being warmer compared to southern-facing slopes which results is a highly variable solar illumination geometry and angle of incidence PAR.

Since both the Pongola and Sezela sampled fields had variation in sugarcane cultivars (Supplementary Material 1) and the Pongola fAPAR models performed significantly (this term is consistently used in this article to signify statistical significance) better than that of Sezela, we can assume that the environmental, geographical and farming practice variations had a bigger impact than the variation in cultivars on the modelling of fAPAR.

The relatively poor performance (mean RMSE of more than 13.7% for the combined study areas) of the sugarcane fAPAR models developed in other regions or based on different crops (Morel et al. (2014), Zhang et al. (2015) and Bastiaanssen and Ali (2003)) suggests that such models are not always transferable. As with the models generated in the present study, the existing models performed substantially better in Pongola compared to Sezela. For instance, the model by Morel et al. (2014) performed reasonably well in Pongola (RMSE of 9.81%), but in Sezela it returned the second-highest error rates (17.16%) of all the models tested. This further emphasises the challenges of implementing fAPAR modelling in diverse areas such as Sezela. Given these results and, because all of the related regression model coefficient values (slopes, intercept) were significantly different, re-parameterization is suggested to achieve the best possible results for a unique area, when deriving fAPAR values empirically.

The SWIR-based variables played an important role in the models generated from the in situ data. According to Curran (1989), the SWIR region of the electromagnetic spectrum is sensitive to a number of foliage chemicals, including sugars and starches. In addition, the $SWIR^2$ band is known to respond to the presence of proteins, nitrogen and cellulose. This wider chemical sensitivity of the $SWIR^2$ band is likely why it featured frequently in the best models. Furthermore, compared to shorter wavelengths,

the SWIR region of the EM spectrum is less affected by atmospheric influences such as aerosols (e.g. smoke and sulphates) (Karnieli et al., 2001; Kaufman and Tanre, 1992) and may explain why the SWIR bands dominated the models produced in Sezela (which has more pronounced atmospheric influences). Although none of the generated models were unaffected by the large variations in cultivation practices and environmental conditions of the two study areas, it would seem that the SWIR-based variables were more robust in modelling fAPAR. Unlike the red and NIR regions of the EM spectrum, little is known of the SWIR capabilities in modelling fAPAR values and should be considered in further research.

The results show that the cubic regression models performed significantly better than the linear and quadratic models. Since the bootstrapping principle was applied in model training and evaluation, overfitting should be minimized in the aggregated result. However, based on the scatter plots it seems that the modelled fAPAR values deviate from what would be expected at certain levels. In particular, the decreasing relationships between the measured fAPAR and NDMI-SWIR^1 (> 0.4 and < -0.2) is of concern. Although the cubic function achieves a better fit at lower (<40) fAPAR levels, it severely underestimates fAPAR at higher (>85) levels. One could thus argue that there is a higher risk with using the cubic model for operational purposes as it would require a good understanding of the feature-specific threshold values, especially in the low and high fAPAR ranges.

The Landsat-8 imagery used in this study proved very useful, but other sources of imagery should be considered in future research. For instance, the use of Sentinel-2 imagery (instead of, or in addition to Landsat-8) will reduce the average period between image acquisition and in situ measurement dates as it has (since mid-2017) a 5-day revisit time (compared to the 16-day revisit time of Landsat-8). Shorter periods between in situ measurements and image dates will likely strengthen the models.

5 CONCLUSION

In this study, a range of existing and new fAPAR models were generated from multispectral (Landsat-8) data using regression and machine learning. The models were applied in two large and very diverse sugarcane growing regions of South Africa, namely the Pongola and Sezela mill supply areas situated in northern and southern Kwazulu-Natal respectively. Based on the findings we conclude that: 1) existing NDVI-based fAPAR models (developed in other regions) were not as robust as the models generated in this study; 2) SWIR-based models seem to be more robust (stable), with AFRI and NDMI based on SWIR^1 performing consistently well; and 3) fAPAR models should preferably always be calibrated with local in situ data for best performance.

6 ACKNOWLEDGEMENTS

We gratefully acknowledge financial support from SA sugarcane farmers and millers' through the SA Sugar Association, and the field work by SASRI technicians. We also thank LinguaFix (https://www.linguafix.net/) for their valuable editing and proofreading services.

7 REFERENCES

Bappel, Begue, Martine, Pellegrino, Siegmund, 2005. Assimilation of a biophysical parameter estimated by remote sensing using SPOT 4&5 data into a sugarcane yield forecasting model, in: Proc. ISSCT.

Baret, F., Guyot, G., Major, D.J., 1989. Crop biomass evaluation using radiometric measurements. Photogrammetria 43, 241–256. https://doi.org/10.1016/0031-8663(89)90001-X

Baret, F., Hagolle, O., Geiger, B., Bicheron, P., Miras, B., Huc, M., Berthelot, B., Niño, F., Weiss, M., Samain, O., Roujean, J.L., Leroy, M., 2007. LAI, fAPAR and fCover CYCLOPES global products derived from VEGETATION. Remote Sens. Environ. 110, 275–286. https://doi.org/10.1016/j.rse.2007.02.018

Bastiaanssen, W.G.., Ali, S., 2003. A new crop yield forecasting model based on satellite measurements applied across the Indus Basin. Agric. Ecosyst. Environ. 94, 321–340. https://doi.org/10.1016/S0167-8809(02)00034-8

Bausch, W.C., 1993. Soil background effects on reflectance-based crop coefficients for corn. Remote Sens. Environ. 46, 213–222. https://doi.org/10.1016/0034-4257(93)90096-G

Ben-Zeev, E., Karnieli, A., Agam, N., Kaufman, Y., Holben, B., 2006. Assessing vegetation condition in the presence of biomass burning smoke by applying the Aerosol-free Vegetation Index (AFRI) on MODIS images. Int. J. Remote Sens. 27, 3203–3221. https://doi.org/10.1080/01431160500177380

Bezuidenhout, C.N., Singels, A., 2007. Operational forecasting of South African sugarcane production: Part 1 – System description. Agric. Syst. 92, 23–38. https://doi.org/10.1016/j.agsy.2006.02.001

Breiman, L., 2001. Random Forests. Mach. Learn. 45, 5–32. https://doi.org/10.1023/A:1010933404324

Breiman, L., Friedman, J., Stone, C.J., Olshen, R.A., 2017. Classification and regression trees Regression trees, Nature methods. Wadsworth & Brooks, Monterey, CA. https://doi.org/10.1002/widm.8

Campbell, J.A., Robertson, M.J., Grof, C.P.L., 1998. Temperature effects on node appearance in sugarcane. Aust. J. Plant Physiol. 25, 815. https://doi.org/10.1071/PP98040

Ceccato, P., Flasse, S., Tarantola, S., Jacquemoud, S., Grégoire, J.M., 2001. Detecting vegetation leaf water content using reflectance in the optical domain. Remote Sens. Environ. 77, 22–33. https://doi.org/10.1016/S0034-4257(01)00191-2

Chuvieco, E., Huete, A., 2010. Fundamentals of satellite remote sensing. Taylor & Francis, Boca Raton.

Clevers, J.G.P.W., Vonder, O.W., Jongschaap, R.E.E., Desprats, J.-F., King, C., Prévot, L., Bruguier, N., 2002. Using SPOT data for calibrating a wheat growth model under mediterranean conditions. Agronomie 22, 687–694. https://doi.org/10.1051/agro:2002038

Curran, P.J., 1989. Remote sensing of foliar chemistry. Remote Sens. Environ. 30, 271–278. https://doi.org/10.1016/0034-4257(89)90069-2

D'Agostino, R., Pearson, E.S., 1973. Tests for departure from normality. Empirical results for the distributions of b 2 and √ b 1. Biometrika 60, 613–622. https://doi.org/10.1093/biomet/60.3.613

Daughtry, C.S.T., Gallo, K.P., Goward, S.N., Prince, S.D., Kustas, W.P., 1992. Spectral estimates of absorbed radiation and phytomass production in corn and soybean canopies. Remote Sens. Environ. 39, 141–152. https://doi.org/10.1016/0034-4257(92)90132-4

De Silva, A.L.C., De Costa, W.A.J.M., 2012. Growth and Radiation Use Efficiency of Sugarcane Under Irrigated and Rain-fed Conditions in Sri Lanka. Sugar Tech 14, 247–254. https://doi.org/10.1007/s12355-012-0148-y

De Wit, A., Baruth, B., Boogaard, H., van Diepen, K., van Kraalingen, D., Micale, F., te Roller, J., Supit, I., van den Wijngaart, R., 2010. Using ERA-INTERIM for regional crop yield forecasting in Europe. Clim. Res. 44, 41–53. https://doi.org/10.3354/cr00872

Epiphanio, J.C.N., Huete, A.R., 1995. Dependence of NDVI and SAVI on sun/sensor geometry and its effect on fAPAR relationships in Alfalfa. Remote Sens. Environ. 51, 351–360. https://doi.org/10.1016/0034-4257(94)00110-9

Everingham, Y.., Muchow, R.., Stone, R.., Inman-Bamber, N.., Singels, A., Bezuidenhout, C.., 2002. Enhanced risk management and decision-making capability across the sugarcane industry value chain based on seasonal climate forecasts. Agric. Syst. 74, 459–477. https://doi.org/10.1016/S0308-521X(02)00050-1

Everingham, Y.L., Smyth, C.W., Inman-Bamber, N.G., 2009. Ensemble data mining approaches to forecast regional sugarcane crop production. Agric. For. Meteorol. 149, 689–696. https://doi.org/10.1016/j.agrformet.2008.10.018

Fang, H., Liang, S., Hoogenboom, G., 2011. Integration of MODIS LAI and vegetation index products with the CSM-CERES-Maize model for corn yield estimation. Int. J. Remote Sens. 32, 1039–1065. https://doi.org/10.1080/01431160903505310

FAO, 2018. FAOSTAT [WWW Document].

Fensholt, R., Sandholt, I., 2003. Derivation of a shortwave infrared water stress index from MODIS near- and shortwave infrared data in a semiarid environment. Remote Sens. Environ. 87, 111–121. https://doi.org/10.1016/j.rse.2003.07.002

Gallo, K.P., Daughtry, C.S.T., 1986. Techniques for Measuring Intercepted and Absorbed Photosynthetically Active Radiation in Corn Canopies1. Agron. J. 78, 752. https://doi.org/10.2134/agronj1986.00021962007800040039x

Gallo, K.P., Daughtry, C.S.T., Wiegand, C.L., 1993. Errors in Measuring Absorbed Radiation and Computing Crop Radiation Use Efficiency. Agron. J. 85, 1222. https://doi.org/10.2134/agronj1993.00021962008500060024x

Gao, B., 1996. NDWI—A normalized difference water index for remote sensing of vegetation liquid water from space. Remote Sens. Environ. 58, 257–266. https://doi.org/10.1016/S0034-4257(96)00067-3

Gilbertson, J.K., Kemp, J., van Niekerk, A., 2017. Effect of pan-sharpening multi-temporal Landsat 8 imagery for crop type differentiation using different classification techniques. Comput. Electron. Agric. 134, 151–159. https://doi.org/10.1016/j.compag.2016.12.006

Gitelson, A.A., Kaufman, Y.J., Merzlyak, M.N., 1996. Use of a green channel in remote sensing of global vegetation from EOS-MODIS. Remote Sens. Environ. 58, 289–298. https://doi.org/10.1016/S0034-4257(96)00072-7

Gitelson, A.A., Peng, Y., Huemmrich, K.F., 2014. Relationship between fraction of radiation absorbed by photosynthesizing maize and soybean canopies and NDVI from remotely sensed data taken at close range and from MODIS 250m resolution data. Remote Sens. Environ. 147, 108–120. https://doi.org/10.1016/j.rse.2014.02.014

Haboudane, D., Miller, J.R., Pattey, E., Zarco-Tejada, P.J., Strachan, I.B., 2004. Hyperspectral vegetation indices and novel algorithms for predicting green LAI of crop canopies: Modeling and validation in the context of precision agriculture. Remote Sens. Environ. 90, 337–352. https://doi.org/10.1016/j.rse.2003.12.013

Hatfield, J.L., Asrar, G., Kanemasu, E.T., 1984. Intercepted photosynthetically active radiation estimated by spectral reflectance. Remote Sens. Environ. 14, 65–75. https://doi.org/10.1016/0034-4257(84)90008-7

Huang, J., Tian, L., Liang, S., Ma, H., Becker-Reshef, I., Huang, Y., Su, W., Zhang, X., Zhu, D., Wu, W., 2015. Improving winter wheat yield estimation by assimilation of the leaf area index from Landsat TM and MODIS data into the WOFOST model. Agric. For. Meteorol. 204, 106–121. https://doi.org/10.1016/j.agrformet.2015.02.001

Huete, A.R., 1988. A Soil-Adjusted Vegetation Index (SAVI). Remote Sens. Environ. 25, 295–309.

Huete, A R, 1988. A soil-adjusted vegetation index (SAVI). Remote Sens. Environ. 25, 295–309. https://doi.org/10.1016/0034-4257(88)90106-X

Huete, A.R., Justice, C., van Leeuwen, W., 1996. MODIS vegetation index (mod13). Algorithn theoretical basis document. Greenbelt, Maryland, USA.

Inman-Bamber, N.G., 1994. Temperature and seasonal effects on canopy development and light interception of sugarcane. F. Crop. Res. 36, 41–51. https://doi.org/10.1016/0378-4290(94)90051-5

Jarmain, C., Singels, A., Bastidas-Obando, E., Paraskevopoulos, A., Olivier, F., Laan, M. Van Der, Taverna-turisan, D., Dlamini, M., Munch, Z., Bastiaanssen, W., Annandale, J., Everson, C., Savage, M., Walker, S., 2014. Water use efficiency of selected irrigated crops determined with satellite imagery. Pretoria.

Jiang, Z., Huete, A.R., Chen, J., Chen, Y., Li, J., Yan, G., Zhang, X., 2006. Analysis of NDVI and scaled difference vegetation index retrievals of vegetation fraction. Remote Sens. Environ. 101, 366–378. https://doi.org/10.1016/j.rse.2006.01.003

Jiang, Z., Huete, A.R., Didan, K., Miura, T., 2008. Development of a two-band enhanced vegetation index without a blue band. Remote Sens. Environ. 112, 3833–3845. https://doi.org/10.1016/j.rse.2008.06.006

Jin, H., Li, A., Wang, J., Bo, Y., 2016. Improvement of spatially and temporally continuous crop leaf area index by integration of CERES-Maize model and MODIS data. Eur. J. Agron. 78, 1–12. https://doi.org/10.1016/j.eja.2016.04.007

Jin, S., Sader, S.A., 2005. Comparison of time series tasseled cap wetness and the normalized difference moisture index in detecting forest disturbances. Remote Sens. Environ. 94, 364–372. https://doi.org/10.1016/j.rse.2004.10.012

Jin, X., Kumar, L., Li, Z., Feng, H., Xu, X., Yang, G., Wang, J., 2018. A review of data assimilation of remote sensing and crop models. Eur. J. Agron. 92, 141–152. https://doi.org/10.1016/j.eja.2017.11.002

Jin, Z., Azzari, G., Lobell, D.B., 2017. Improving the accuracy of satellite-based high-resolution yield estimation: A test of multiple scalable approaches. Agric. For. Meteorol. 247, 207–220. https://doi.org/10.1016/j.agrformet.2017.08.001

Joel, G., Gamon, J.A., Field, C.B., 1997. Production efficiency in sunflower: The role of water and nitrogen stress. Remote Sens. Environ. 62, 176–188. https://doi.org/10.1016/S0034-4257(97)00093-X

Jones, H.G., Vaughan, R.A., 2010. Remote sensing of vegetation: Principles, techniques, and applications. Oxford Univeristy Press, New York.

Jordan, C.F., 1969. Derivation of Leaf-Area Index from Quality of Light on the Forest Floor. Ecology 50,

663–666. https://doi.org/10.2307/1936256

Karnieli, A., Kaufman, Y.J., Remer, L., Wald, A., 2001. AFRI -- aerosol free vegetation index. Remote Sens. Environ. 77, 10.

Kaufman, Y.J., Tanre, D., 1992. Atmospherically resistant vegetation index (ARVI) for EOS-MODIS. IEEE Trans. Geosci. Remote Sens. 30, 261–270. https://doi.org/10.1109/36.134076

Lebourgeois, V., Dupuy, S., Vintrou, É., Ameline, M., Butler, S., Bégué, A., 2017. A Combined Random Forest and OBIA Classification Scheme for Mapping Smallholder Agriculture at Different Nomenclature Levels Using Multisource Data (Simulated Sentinel-2 Time Series, VHRS and DEM). Remote Sens. 9, 259. https://doi.org/10.3390/rs9030259

Li, Z., Wang, J., Xu, X., Zhao, C., Jin, X., Yang, G., Feng, H., 2015. Assimilation of two variables derived from hyperspectral data into the DSSAT-CERES model for grain yield and quality estimation. Remote Sens. 7, 12400–12418. https://doi.org/10.3390/rs70912400

Morel, J., Bégué, A., Todoroff, P., Martiné, J.F., Lebourgeois, V., Petit, M., 2014. Coupling a sugarcane crop model with the remotely sensed time series of fIPAR to optimise the yield estimation. Eur. J. Agron. 61, 60–68. https://doi.org/10.1016/j.eja.2014.08.004

Morell, F.J., Yang, H.S., Cassman, K.G., Wart, J. Van, Elmore, R.W., Licht, M., Coulter, J.A., Ciampitti, I.A., Pittelkow, C.M., Brouder, S.M., Thomison, P., Lauer, J., Graham, C., Massey, R., Grassini, P., 2016. Can crop simulation models be used to predict local to regional maize yields and total production in the U.S. Corn Belt? F. Crop. Res. 192, 1–12. https://doi.org/10.1016/j.fcr.2016.04.004

Moulin, S., Bondeau, A., Delecolle, R., 1998. Combining agricultural crop models and satellite observations: From field to regional scales. Int. J. Remote Sens. 19, 1021–1036. https://doi.org/10.1080/014311698215586

Myneni, R.B., 1997. Estimation of global leaf area index and absorbed par using radiative transfer models. IEEE Trans. Geosci. Remote Sens. 35, 1380–1393. https://doi.org/10.1109/36.649788

Nguy-Robertson, A., Gitelson, A., Peng, Y., Viña, A., Arkebauer, T., Rundquist, D., 2012. Green leaf area index estimation in maize and soybean: Combining vegetation indices to achieve maximal sensitivity. Agron. J. 104, 1336–1347. https://doi.org/10.2134/agronj2012.0065

Nikolakopoulos, K.G., 2008. Comparison of Nine Fusion Techniques for Very High Resolution Data. Photogramm. Eng. Remote Sens. 74, 647–659. https://doi.org/10.14358/PERS.74.5.647

Oliphant, T.E., 2007. Python for Scientific Computing. Comput. Sci. Eng. 9, 10–20. https://doi.org/10.1109/MCSE.2007.58

Pedregosa, F., Varoquaux, G., Gramfort, A., Michel, V., Thirion, B., Grisel, O., Blondel, M., Prettenhofer, P., Weiss, R., Dubourg, V., Vanderplas, J., Passos, A., Cournapeau, D., Brucher, M., Perrot, M., Duchesnay, É., 2012. Scikit-learn: Machine Learning in Python. J. Mach. Learn. Res. 12, 2825–2830. https://doi.org/10.1007/s13398-014-0173-7.2

Rahman, M.M., Lamb, D.W., 2017. The role of directional LAI in determining the fAPAR–NDVI relationship when using active optical sensors in tall fescue (Festuca arundinacea) pasture. Int. J. Remote Sens. 38, 3219–3235. https://doi.org/10.1080/01431161.2017.1292069

Richter, R., 2004. ATCOR: Atmospheric and topographic correction. DLR - Gerrman Aerospaice Center.

Ridao, E., Conde, J.R., Mínguez, M.I., 1998. Estimating fAPAR from nine vegetation indices for irrigated and nonirrigated faba bean and semileafless pea canopies. Remote Sens. Environ. 66, 87–100. https://doi.org/10.1016/S0034-4257(98)00050-9

Rouse, J.W., 1973. Monitoring the vernal advancement and retrogradation (green wave effect) of natural vegetation.

Scikit-learn, 2016. Scikit-learn user guide - release 0.18.1.

Singels, A., Donaldson, R.A., 2000. A simple model of unstressed sugarcane canopy development. Proc. South African Sugar Technol. Assoc. 74, 151–154.

Singels, A., Paraskevopoulos, A., 2017. The Canesim® sugarcane model: Scientific documentation. Mount Edgecombe.

Singels, A., Smit, M.A., 2002. the Effect of Row Spacing on an Irrigated Plant Crop of Sugarcane Variety Nco376. Proc. South African Sugar Technol. Assoc. 94–105.

Singels, A., Smit, M.A., Redshaw, K.A., Donaldson, R.A., 2005. The effect of crop start date, crop class and cultivar on sugarcane canopy development and radiation interception. F. Crop. Res. 92, 249–260. https://doi.org/10.1016/j.fcr.2005.01.028

Wilcox, R.R., 2001. Fundamentals of Modern Statistical Methods. Springer New York, New York, NY. https://doi.org/10.1007/978-1-4757-3522-2

Zhang, H., Anderson, R.G., Wang, D., 2015. Satellite-based crop coefficient and regional water use estimates for Hawaiian sugarcane. F. Crop. Res. 180, 143–154. https://doi.org/10.1016/j.fcr.2015.05.023

Zhang, Y.Z.Y., 2002. A new automatic approach for effectively fusing Landsat 7 as well as IKONOS images. IEEE Int. Geosci. Remote Sens. Symp. 4, 2429–2431. https://doi.org/10.1109/IGARSS.2002.1026567

Zhou, M.M., Singels, A., Savage, M.J., 2003. Physiological Parameters for Modelling Differences in Canopy Development Between. Proc. South African Sugar Technol. Assoc. 610–621.

Supplementary Material 1 Cropping details for the validation fields

Mill area	*Field code	Field Size (ha)	Variety	Row spacing (m) and configuration	Crop class on Jun-15)	Crop Start date	Harvest date			Cane yield (t/ha)			Harvesting Method	Irrigation System
							2014	2015	2016	2014	2015	2016		
Pongola	P1	7.0	N41	1.4 SL	R4	19-May-13	04-Jul	07-Jun	10-Jun	96	81	70	B	SP
Pongola	P2	5.7	N41	1.4 SL	R6	28-Apr-13	20-May	04-May	04-Jun	67	88	75	B	DL
Pongola	P3	4.2	N23	1.2 SL	R9	20-Jul-13	01-Aug	05-Jul-05	20-Jun	108	104	58	B	DL
Pongola	P4	13.3	N36	1.8 x 0.6 TL	R2	15-Mar-13	28-Jun	29-Jun	22-Aug	167	132	83	B	CP
Pongola	P5	13.2	N53	1.8 x 0.6 TL	R2	15-Jan-13	04-Apr	05-May	06-Jul	200	153	65	B	CP
Pongola	P6	9.4	N53	1.8 x 0.4 TL	P	28-Feb-15	-	-	02-Jun	-	-	194	B	D
Pongola	P7	9.0	N41	1.8 x 0.6 TL	R1	11-Apr-14	-	10-Apr	22-Jun	-	144	87	B	D
Pongola	P8	4.0	N41	1.4 SL	R2	13-May-13	14-Jun	15-May	21-May	67	-	55	B	SP
Pongola	P9	7.0	N53	1.8 x 0.5 TL	P	07-Mar-15	-	-	24-May	-	-	33	B	SP
Pongola	P10	10.6	N53	1.8 x 0.5 TL	R2	01-Mar-13	22-May	15-Jun	03-Aug	102	93	14	B	CP
Sezela	S1	13.4	N39	1.2 SL	R1	03-Dec-13	-	10-Apr	25-Jun	-	60	79	B	RF
Sezela	S2	7.1	N39	1.0 SL	R3	01-Oct-13	01-Oct	15-Oct	-	50	-	-	B	RF
Sezela	S3	6.5	N12	1.0 SL	R1	15-Oct-13	-	28-Jul	-	-	101	-	B	RF
Sezela	S4	4.2	N12	1.5 SL	R2	01-Nov-13	07-Sep	-	10-May	99	-	73	B	RF
Sezela	S5	10.6	N12	1.5 SL	R1	01-Oct-13	07-Sep	-	16-Jun	66	-	95	B	RF
Sezela	S6	31.5	N47	1.2 SL	R2	05-Jul-13	20-Jul	18-Sep		44	54	-	G	RF
Sezela	S7	12.5	N41	1.2 SL	R1	12-Oct-13	-	30-Apr	23-Jun	-	62	80	G	RF
Sezela	S8	24.8	N12	1.0 SL	R13	26-Jun-13	22-Sep	28-Aug	-	41	31	-	B	RF
Sezela	S9	28.9	N12	1.0 SL	R8	15-Nov-13	-	08-Apr	08-Jul	-	50	62	B	RF
Sezela	S10	15.0	N12	1.0 SL	R14	02-Dec-13	21-Nov	-	21-May	47	-	76	G	RF

* Actual field numbers and grower information have been kept confidential

B = Burnt harvest; CP = Centre Pivot; D = Drip; DL = Drag Line; G = Green harvest; P = Plant Crop; R = Ratoon No.; RF = Rainfed; SL = Single Lines; SP = Semi Permanent; TL = Tram Lines

Supplementary Material 2 Ground sampling dates for the different validation fields

Mill area	Field Code	Jun-15	Jul-15	Aug-15	Sep-15	Oct-15	Nov-15	Dec-15	Jan-16	Feb-16	Mar-16	Apr-16	May-16	Jun-16	Jul-16	Aug-16	Sep-16	Oct-16
Pongola	P1		✓	✓	✓	✓	✓	✓	✓	✓	✓				✓	✓	✓	✓
Pongola	P2		✓	✓	✓	✓	✓	✓	✓	✓	✓				✓	✓	✓	✓
Pongola	P3		✓	✓	✓	✓	✓	✓	✓	✓	✓	✓	✓	✓	✓	✓	✓	✓
Pongola	P4		✓	✓	✓	✓	✓	✓	✓	✓	✓	✓					✓	✓
Pongola	P5	✓	✓	✓	✓	✓	✓	✓	✓	✓	✓	✓	✓	✓	✓	✓	✓	✓
Pongola	P6	✓	✓	✓	✓	✓	✓	✓	✓	✓	✓	✓	✓	✓	✓	✓	✓	✓
Pongola	P7	✓	✓	✓	✓	✓	✓									✓	✓	✓
Pongola	P8		✓	✓	✓	✓	✓			✓		✓		✓	✓		✓	✓
Pongola	P9	✓	✓	✓	✓	✓	✓	✓	✓	✓	✓	✓	✓	✓	✓	✓	✓	✓
Pongola	P10		✓	✓	✓	✓	✓			✓						✓	✓	
Sezela	S1		✓	✓	✓	✓	✓		✓	✓	✓	✓			✓	✓	✓	✓
Sezela	S2		✓	✓	✓	✓	✓		✓	✓	✓	✓	✓	✓	✓			
Sezela	S3		✓	✓	✓	✓	✓			✓	✓	✓	✓					
Sezela	S4		✓	✓	✓	✓	✓			✓	✓		✓	✓	✓	✓	✓	
Sezela	S5		✓	✓	✓	✓	✓			✓				✓	✓	✓	✓	
Sezela	S6		✓	✓	✓	✓	✓		✓	✓	✓	✓	✓	✓	✓			
Sezela	S7		✓	✓	✓	✓	✓		✓	✓	✓	✓			✓	✓	✓	✓
Sezela	S8		✓	✓	✓	✓	✓		✓	✓	✓		✓	✓	✓	✓	✓	
Sezela	S9		✓	✓	✓	✓	✓		✓	✓	✓		✓	✓	✓	✓	✓	
Sezela	S10		✓	✓	✓	✓	✓		✓	✓	✓		✓	✓	✓	✓		

Supplementary Material 3 Summary of acquired Landsat-8 images with path row numbers and indication of cloud interference

Pongola	Sezela (Path/Row)
Path/Row: 168/79	Path/Row: 168/81
2015-05-13*	2015-05-13
2015-05-29	2015-05-29
2015-06-14	2015-06-14
2015-07-16	2015-08-01
2015-08-01	2015-08-17
2015-08-17	2015-09-02
2015-10-04*	2015-10-04
2015-10-20	2015-10-20
2015-11-05	2015-11-05
2016-02-09	2016-01-24*
2016-03-28	2016-03-12*
2016-04-29	2016-03-28*
2016-05-31	2016-04-29
2016-07-18	2016-05-15
2016-08-03	2016-05-31
2016-08-19	2016-07-18
2016-09-20	2016-08-03*
2016-10-06	2016-09-20
2016-10-22*	2016-10-06

* Landast images affected by cloud and omitted from analysis

Supplementary Material 4 Landsat-8 OLI technical specifications

Landsat-8 Band	Description	Wavelength (μm)	Spatial resolution
1	Coastal aerosol	0.43 - 0.45	30 m
2	Blue	0.45 - 0.51	30 m
3	Green	0.53 - 0.59	30 m
4	Red	0.64 - 0.67	30 m
5	Near Infrared (NIR)	0.85 - 0.88	30 m
6	Cirrus	1.36 - 1.38	30 m
7	Short Wave Infrared 1 (SWIR[1])	1.56 – 1.65	30 m
8	Short Wave Infrared 2 (SWIR[2])	2.10 - 2.29	30 m
Pan	Panchromatic	0.503 – 0.676	15 m